Unified Compressive Sensing Paradigm for the Random Demodulator and Compressive Multiplexer Architectures

Journal Item

IET Signal Processing

Research Article

IET Journals
The Institution of Engineering and Technology

Unified compressive sensing paradigm for the random demodulator and compressive multiplexer architectures

ISSN 1751-9675
Received on 16th December 2019
Revised 19th June 2020
Accepted on 21st July 2020
doi: 10.1049/iet-spr.2019.0589
www.ietdl.org

Dimitrios Karampoulas[1], Laurence S. Dooley[2], Soraya Kouadri Mostefaoui[2] ✉

[1]*Cobham Aerospace Connectivity, Bournemouth International Airport, Dorset, UK*
[2]*School of Computing & Communications, The Open University, Milton Keynes, UK*
✉ *E-mail: soraya.kouadri@open.ac.uk*

Abstract: A major challenge in spectrum sensing for *cognitive radio* (CR) applications is the very high sampling rates involved, which imposes significant demands on the signal acquisition technology. This has given impetus to applying *compressive sensing* (CS) as a sub-Nyquist sampling paradigm for CR-type wireless signals which exhibit sparsity in certain domains. CS architectures like the *random demodulator* (RD) and *compressive multiplexer* (CM) can be used for CR spectral sensing, though both are inherently restricted in terms of the signal classes they can effectively process. To address these limitations, this study presents two unified RD and CM-based CS architectures that seamlessly integrate precolouring and the *multitaper* spectral estimator into their respective structures to facilitate efficient sensing of both digitally modulated and narrowband signals, along with popular CR-access technologies like *orthogonal frequency division multiplexing*. A significant feature of these unified CS architectures is they do not require a priori knowledge of either the input signal or modulation scheme, while a tristate spectral classifier is introduced to afford notably enhanced spectrum access opportunities for unlicensed secondary users. A critical performance evaluation corroborates that both unified architectures demonstrate consistently superior CS results and robustness across a broad range of CR-type signals, modulations and access technologies.

1 Introduction

Wireless communications have experienced rapid growth in the past decade and as new technologies, services, devices and applications emerge [1, 2], the corollary is an insatiable demand for ever-higher data-rates, a mandate which renders access to finite spectral resources a significant challenge. This situation is compounded by the spectral licensing regime of regulatory bodies [3], which gives exclusive access to licensed or primary users (PUs), with no violation permitted by unlicensed or secondary users (SUs).

Despite spectrum scarcity and inflexible regulations, the available spectrum is underutilised [4, 5], with frequency usage between 30 and 3 GHz, typically ranging from 15 to 85% [4]. Cognitive radio (CR) networks [6–9], especially when based on cooperative or spectrum sharing communication schemes [10, 11], afford the potential to alleviate this spectral underutilisation. A crucial requirement for CR networks is spectrum sensing, which is the ability to reliably identify underutilised bands [6]. While spectrum estimation methods can facilitate CR sensing, major challenges arise, such as the very high sampling rates and stringent timing requirements involved [12, 13].

Compressive sensing (CS) is a sampling paradigm for signal acquisition [14, 15]. An essential prerequisite for efficient CS is the signal of interest must be sparse in some domain, i.e. Fourier [16, 17], so it can be represented by a smaller number of significant frequency components than its bandwidth implies [14]. This is common in wireless networks, where signal sparsity is a natural corollary of spectrum underutilisation. CS requires the availability of a relatively small number of non-adaptive measurements [14] to reconstruct sparse signals, hence the attractiveness of CS as a feasible solution to the aforementioned sampling and timing problems appertaining to CR networks [18, 19].

Several popular CS architectures exist including the random demodulator (RD) [20], the modulated wideband converter (MWC) [21], the compressive multiplexer (CM) [22], the random convolution [23] and random filtering [24], with the RD and MWC being implemented as hardware prototypes [25, 26].

The RD is especially effective in recovering discrete multi-tone signals, characterised by being bandlimited, periodic and sparse [20]. Due to signal sparsity, the number of tones is small compared with the bandlimited version with examples including narrowband modulation schemes, acoustic and musical signals, frequency-hopping modulation schemes and slow-varying chirps [20]. In wireless applications, where multiband signals with continuous spectra are often encountered, the RD often requires a larger number of tones to achieve suitable signal approximation [21], with a resulting impact on the computational overheads of both the signal sampling and recovery stages.

Various enhancements to the original RD architecture have been proposed, though all retain the basic underlying structure. For example, in [27, 28] a parallel-segmented RD architecture exhibits improved sensing performance but at the cost of increased hardware complexity, while multiple RD signal acquisition structures are utilised in [29] to lower the sampling rate, but again higher complexity is incurred due to windowing and SU synchronisation issues.

Superior spectrum estimation techniques are not incorporated in these RD enhancements, so the architectures are constrained by the innate limitations of the periodogram [30, 31], while input signals are not processed to exploit propitious features that could enhance CS performance. One RD model [32] uses the *multitaper* (MT) spectral estimator in combination with singular value decomposition, to improve occupied band detection but because the number of RD structures must equal the number of Slepian sequences, this significantly impacts upon both the hardware and computational complexity. Other RD solutions address issues relating to non-ideal chipping sequences [33, 34], though these require a priori knowledge of the input signal, which is not always viable in wireless communications.

In [35], the MT spectrum estimator has been seamlessly integrated into the RD model to increase signal sparsity for narrowband modulation schemes like amplitude modulation (AM) and chirps, and to improve CS performance, without incurring the extra system overheads identified in [32].

In [36, 37], an *autoregressive* (AR) filter is introduced to precolour digitally modulated signals to enhance sparsity by emphasising dominant frequencies and attenuating weaker ones, while in [38] precolouring has been seamlessly integrated into the

RD recovery stage using a *precolouring matrix* (PM) to avoid imposing any pre-processing requirements on the input.

Despite embedding filtering and spectrum estimation techniques into the RD model, each approach is limited to specific signal and modulation types. The AR-based architecture work applies to digitally modulated signals and does not exploit the favourable properties of the MT method when precolouring is ineffectual. Conversely, the MT-based RD architecture is only suitable for narrowband modulations. Furthermore, in [36–38], the AR-based architecture has not been investigated for popular CR network access schemes like *orthogonal frequency division multiplexing* (OFDM), which is defined in both the 4G Long-Term Evolution (LTE) [39] and IEEE 802.11.af [40] standards. Moreover, the effectiveness of precolouring and MT method for sparsity enhancement has only been analysed within an RD context and not extended and critically evaluated on alternative CS models such as the CM.

Another issue in these various RD architectures is the spectrum sensing requirement for CR purposes, involving spectral band detection and classification [3, 8]. Traditional spectrum classification uses a binary hypothesis test [3, 41], implying either occupied (black) or vacant (white) bands. However, there are also so-called *grey states* which indicate a band partially occupied by interferers, noise or very weak PU signals. These can also be exploited for CR purposes, since they are potentially vacant and available for SU access [8]. This motivated the investigation into how CS architectures can effectively perform spectrum sensing by allowing the existence of three classification states rather than normal two.

From a CR network SU perspective, it is advantageous to have a compressive spectrum sensing strategy that covers as wide a range of CR-type signals, modulation and access methods as possible. This paper presents a novel unified RD-based CS model (UNI-RD) that can process both digitally modulated and narrowband signals as well as popular CR-based access schemes like OFDM, without crucially the prerequisite for a priori knowledge of either the modulation scheme or input signal. The UNI-RD architecture is critically evaluated and benchmarked against existing AR and MT-based CS models. Additionally, its spectral classification performance is enhanced by introducing a tristate classifier, which affords significant new opportunities for SU access. Finally, the unified architecture is extended to the CM CS architecture (UNI-CM) to critically appraise its applicability as a generic CR spectrum sensing solution. Quantitative results confirm that for the gamut of CR-type signals and access schemes, the unified architectures consistently demonstrate superior comparative CS performance and robustness. They also confirm that both precolouring and MT estimation method can be seamlessly embedded into other CS architectures to improve their respective spectrum sensing capability.

The remaining part of this paper is organised as follows: Section 2 briefly reviews the AR and MT-based RD architectures before introducing the unified RD-based CS architecture. Section 3 examines the integration of precolouring and the MT method into the CM architecture, while Section 4 details the new tristate spectral classifier. A detailed critical results analysis is presented in Section 5, with some concluding comments provided in Section 6.

2 Unified RD-based CS model

2.1 Review of AR and MT-based RD architectures

In the basic RD structure, a frequency sparse input signal $x(t)$ is modulated by a pseudorandom chipping sequence with values ±1, at the Nyquist rate N before being low-pass filtered and then subsampled at a sub-Nyquist rate $M < N$ to yield a discrete set of measurements $\boldsymbol{y}$ of length M [20, 21] such that

$$\boldsymbol{y} = \boldsymbol{A}\boldsymbol{x} = \boldsymbol{A}\boldsymbol{F}^{-1}\boldsymbol{f}, \tag{1}$$

where $\boldsymbol{A}$ is a random $M \times N$ matrix, $\boldsymbol{F}$ is the $N \times N$ *discrete Fourier transform* (DFT) matrix and $\boldsymbol{f}$ is the Fourier representation of $x(n)$. The frequency vector $\boldsymbol{f}$ and subsequent PSD are recovered from the $M \times 1$ measurement vector $\boldsymbol{y}$ by applying suitable l_1 minimisation algorithms to (1) with $\boldsymbol{G} = \boldsymbol{A}\boldsymbol{F}^{-1}$ the recovery matrix [14, 15].

For digital communication schemes, the RD can increase signal sparsity [36] by precolouring the input $x(t)$ using an AR filter [30], so dominant spectral components are emphasised while weaker frequencies outside the occupied bands are attenuated. Applying AR is apposite for spectra with relatively few narrow peaks [30, 42], which is a scenario often encountered in wireless networks, where digitally modulated signals are inherently frequency sparse.

To avoid pre-processing the input signal [36], a PM $\boldsymbol{C}$ is seamlessly integrated into the recovery stage of the RD (*i*PM-RD), so the only PU requirement is the provision of the individual elements of the PM $\boldsymbol{C}$ by the mobile telecommunication providers [36]. The *i*PM-RD model is thus represented as

$$\boldsymbol{y} = \boldsymbol{A}\boldsymbol{x} = \boldsymbol{A}\boldsymbol{C}^{-1}\boldsymbol{F}^{-1}\boldsymbol{f}_C, \tag{2}$$

where $\boldsymbol{f}_C = \boldsymbol{F}\boldsymbol{C}\boldsymbol{x}$ is the recovered PM frequency vector and $\boldsymbol{G}_C$ is the PM recovery matrix. $\boldsymbol{C}$ is a lower triangular Toeplitz invertible matrix with the main diagonal elements being one so it can be completely defined by the first column:

$$\boldsymbol{C} = \begin{bmatrix} 1 & 0 & 0 & . & . & 0 \\ c_1 & 1 & 0 & . & . & 0 \\ c_2 & c_1 & 1 & . & . & 0 \\ . & . & . & . & . & . \\ . & . & . & . & . & . \\ c_{N-1} & c_{N-2} & . & . & . & 1 \end{bmatrix}, \tag{3}$$

where the individual elements c_n are recursively obtained from the AR coefficients by

$$c_n = \sum_{k=1}^{p} \alpha_k c_{n-k}, \tag{4}$$

where $k = 1, 2, \ldots, p$ and $n = 1, 2, \ldots, N-1$

For narrowband modulation schemes, the MT spectral estimator is integrated into the RD to form the MT-RD architecture [35], with an $N \times N$ MT diagonal, invertible matrix $\boldsymbol{S}$ introduced, whose values are determined from the Slepian sequences of the MT spectral estimator and their respective eigenvalues, which in turn, are dependent upon only the signal length N and bandwidth resolution [8]. By exploiting the invertible nature of $\boldsymbol{S}$, the MT frequency vector $\boldsymbol{f}_{\mathrm{MT}}$ of $x(t)$ is derived as [35]

$$\boldsymbol{y} = \boldsymbol{A}\boldsymbol{x} = \boldsymbol{A}\boldsymbol{S}^{-1}\boldsymbol{F}^{-1}\boldsymbol{f}_{\mathrm{MT}} = \boldsymbol{G}_{\mathrm{MT}}\boldsymbol{f}_{\mathrm{MT}}, \tag{5}$$

where $\boldsymbol{G}_{\mathrm{MT}}$ is the multitaper recovery matrix and $\boldsymbol{f}_{\mathrm{MT}} = \boldsymbol{F}\boldsymbol{S}\boldsymbol{x}$, where $\boldsymbol{S}$ has the form

$$\boldsymbol{S} = \begin{bmatrix} s_{00} & 0 & . & . & . & 0 \\ 0 & s_{11} & 0 & . & . & 0 \\ 0 & 0 & s_{22} & . & . & . \\ . & . & . & . & . & . \\ 0 & 0 & . & . & . & s_{N-1N-1} \end{bmatrix}, \tag{6}$$

where s_{kk} are functions of the Slepian sequences and the eigenvalues for $k = 1, 2, \ldots, N-1$. It is assumed, without loss of generality, that the number of Slepian sequences used in all the MT spectral estimator experiments is 10 as in [8], as this offers a pragmatic balance between improved spectral estimation and time complexity.

While lower spectral leakage in the MT-based RD enhances the sparsity of narrowband signals, this is not the case for wideband digitally modulated signals, which are characterised by a main lobe centred about the carrier frequency and side-lobes distributed across the spectrum. As the side-lobes are part of the signal

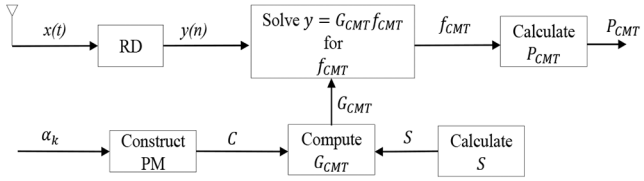

Fig. 1 *Block diagram of the UNI-RD architecture*

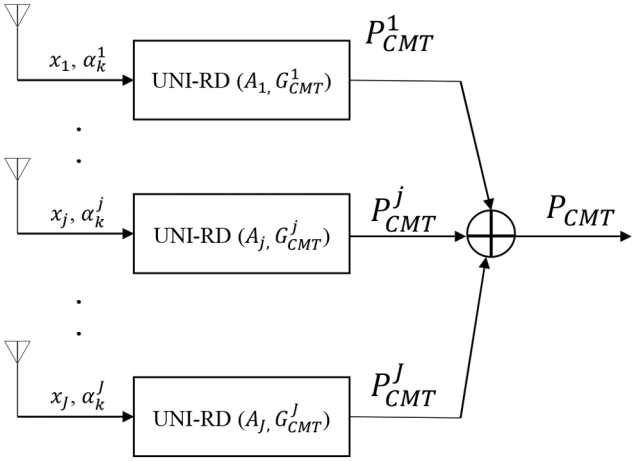

Fig. 2 *Block diagram of the J-channel UNI-RD architecture*

spectrum rather than leakage, the MT method does not suppress them, so little CS performance improvement is achieved and employing the precolouring strategy in (2) is a more pragmatic approach [35]. The *i*PM-RD architecture, however, only uses the AR coefficients for a single PU, so it processes the corresponding signal assigned to a specific PU channel. This means it cannot currently process multiple PUs, which is essential in real-world scenarios, where different spectral bands are utilised by different PU signals using different modulation schemes and access technologies. The corollary from a CR spectrum sensing perspective is that for a CS architecture to fully exploit the sparsity benefits of both precolouring and the MT method, it must be able to simultaneously process different signals with varying modulation and access schemes. This key issue is considered in the next subsection.

2.2 Integration of precolouring and the MT estimator into a unified RD architecture

One approach to achieving a unified mode of operation for the RD is to judiciously select either matrix $\boldsymbol{C}$ or $\boldsymbol{S}$, in (3) or (5), respectively, in the PSD recovery stage. This means the elements of the MT recovery matrix $\boldsymbol{G}_{\text{MT}}$ of MT-RD (5) can be stored offline and reused in a similar way to the recovery matrix $\boldsymbol{G}$ elements [19], so the MT estimator can enhance CS performance for narrowband signals, while having no impact on wideband signals. Conversely, $\boldsymbol{C}$ is signal-dependent, so when there are no AR coefficients, i.e. $\alpha_k = 0$, (3) relaxes to a unitary matrix $\boldsymbol{I}$ and only when $\alpha_\kappa \neq 0$ will precolouring deliver sparsity enhancement.

To integrate the precolouring process into the MT-RD architecture, the corresponding recovery matrix must be determined. In (4), $\boldsymbol{f}_{\text{MT}}$ may be interpreted as the DFT of the MT version of $\boldsymbol{x}$, i.e. $\boldsymbol{x}_{\text{MT}} = \boldsymbol{S}\boldsymbol{x}$, so

$$\boldsymbol{F}_{\text{MT}} = \boldsymbol{F}\boldsymbol{S}\boldsymbol{x} = \boldsymbol{F}(\boldsymbol{S}\boldsymbol{x}) = \boldsymbol{F}\boldsymbol{x}_{\text{MT}}, \tag{7}$$

Using (2) in an analogous manner, $\boldsymbol{f}_C$ is the DFT of the precoloured version of $\boldsymbol{x}$, i.e. $\boldsymbol{x}_C = \boldsymbol{C}\boldsymbol{x}$ so:

$$\boldsymbol{f}_C = \boldsymbol{F}\boldsymbol{C}\boldsymbol{x} = \boldsymbol{F}(\boldsymbol{C}\boldsymbol{x}) = \boldsymbol{F}\boldsymbol{x}_C, \tag{8}$$

From (7) and (8), if precolouring is applied to $\boldsymbol{x}_{\text{MT}}$ then

$$\boldsymbol{x}_{\text{CMT}} = \boldsymbol{C}\boldsymbol{x}_{\text{CMT}} = \boldsymbol{C}\boldsymbol{S}\boldsymbol{x}, \tag{9}$$

where $\boldsymbol{x}_{\text{CMT}}$ is the precoloured version of $\boldsymbol{x}_{\text{MT}}$ so the corresponding DFT becomes

$$\boldsymbol{f}_{\text{CMT}} = \boldsymbol{F}\,\boldsymbol{x}_{\text{CMT}} = \boldsymbol{F}\boldsymbol{C}\boldsymbol{x}_{\text{MT}} = \boldsymbol{F}\boldsymbol{C}\boldsymbol{S}\boldsymbol{x}\,. \tag{10}$$

Thus, in the unified RD structure, signal recovery involves taking the measurement vector $\boldsymbol{y} = \boldsymbol{A}\boldsymbol{x}$ and then deriving the coloured-MT version of $\boldsymbol{x}$ ($\boldsymbol{f}_{\text{CMT}}$) and its corresponding PSD $\boldsymbol{P}_{\text{CMT}} = |\boldsymbol{f}_{\text{CMT}}|^2$ from

$$\boldsymbol{y} = \boldsymbol{A}\boldsymbol{x} = \boldsymbol{A}\boldsymbol{S}^{-1}\boldsymbol{C}^{-1}\boldsymbol{F}^{-1}\boldsymbol{f}_{\text{CMT}} = \boldsymbol{G}_{\text{CMT}}\boldsymbol{f}_{\text{CMT}}, \tag{11}$$

where $\boldsymbol{G}_{\text{CMT}} = \boldsymbol{A}\boldsymbol{S}^{-1}\boldsymbol{C}^{-1}\boldsymbol{F}^{-1}$ is the precolouring-multitaper (PM-MT) recovery matrix and $\boldsymbol{f}_{\text{CMT}}$ is solved, as in (1), by suitable l_1 minimisation algorithms [14]. The PM-RD recovery matrix can be seamlessly integrated into the classic RD leading to the unified RD (UNI-RD) architecture, whose generic block diagram is shown in Fig. 1.

The performance of the UNI-RD architecture is crucially determined by the AR coefficients. If they are zero, PM-MT reduces to the recovery matrix $\boldsymbol{G}_{\text{MT}}$ since there is no precolouring and the benefits of the MT estimator dominate. With non-zero AR coefficients, the PM-MT matrix is weighted by both $\boldsymbol{S}$ and $\boldsymbol{C}$ and the CS advantages of the precolouring are preeminent.

In terms of its computational complexity, the UNI-RD architecture is dependent on the elements of (11). Assuming the availability of the measurement vector $\boldsymbol{y}$, the critical elements are matrices $\boldsymbol{S}$ and $\boldsymbol{C}$. Obviously, the more Slepian sequences used in the MT estimator, the higher the time overhead incurred in solving (11). As for $\boldsymbol{C}$ this is governed by both N and the precolouring filter order p, which is either 4th or 8th order. Moreover, depending on N and p, additional time is incurred to recursively calculate the individual entries of $\boldsymbol{C}$ in (3), while in contrast, the individual elements s_{kk} of $\boldsymbol{S}$ can be calculated offline and stored in a look-up-table within the UNI-RD hardware.

UNI-RD only processes one PU signal channel for a transmitted set of AR coefficients, so in an actual network environment involving multiple signals, parallel UNI-RD architectures must be employed, as shown in Fig. 2. Each branch processes a separate signal with its own set of AR coefficients and as each will have different sampling and recovery matrices, the outputs from each parallel structure are summed together to form the final output $\boldsymbol{P}_{\text{CMT}}$. For J inputs, $\boldsymbol{P}_{\text{CMT}}$ is given by

$$\boldsymbol{P}_{\text{CMT}} = \sum_{j=1}^{J} P_{\text{CMT}}^j, \tag{12}$$

where $\boldsymbol{P}_{\text{CMT}}$ is the PSD for the jth branch of the UNI-RD. Using a higher number of UNI-RD branches give this architecture the ability to sense a wider frequency spectrum, though the trade-off is a commensurate increase in the hardware requirements.

The parallel UNI-RD architecture shown in Fig. 2 is effective for processing multiple OFDM signals, since each OFDM signal is the sum of a large number of closely-spaced orthogonal sub-carriers. Given these signal properties, precolouring can be propitiously applied for sparsity enhancement prior to CS.

The theoretical framework for embedding both precolouring and the MT estimator into UNI-RD has so far, been framed for the RD architecture. In the next section, the unification of these sparsity enhancing mechanisms is extended and critically evaluated for a different CS architecture, namely the *compressive multiplexer*.

3 Precolouring and MT in the CM architecture

CM is an alternative parallel CS architecture, comprising J independent input channels, each of bandwidth $W/2$ and sampled at the Nyquist rate W [22]. As in the RD, each channel $x_j(t)$ is modulated by a pseudorandom chipping sequence $p_j(t)$ with ± 1

values at the Nyquist rate. The vital requirement for sparsity in the CM architecture means signals are jointly sparse over the combined bandwidth, recovery of multiple signals with a total bandwidth of $JW/2$ is feasible at the Nyquist rate W [22]. The nth sample of the summed channel outputs is then

$$y(n) = \sum_{j=1}^{J} \boldsymbol{x}_j(n)\ p_j(n) \tag{13}$$

For N samples, (13) can be expressed in vector form as

$$\boldsymbol{y} = \sum_{j=1}^{J} \boldsymbol{\Phi}_j \boldsymbol{x}_j, \tag{14}$$

where $\boldsymbol{\Phi}_j$ is an $N \times N$ diagonal matrix with the main diagonal being populated by independent identically distributed (i.i.d.) entries from a random distribution, which is typically a Rademacher distribution [22] with values of ± 1.

Both precolouring and the MT spectral estimator are assimilated into the CM architecture in an analogous way to the RD, so for each signal $\boldsymbol{x}_j$, the corresponding PM matrices $\boldsymbol{C}_j$ are calculated, while the elements of the MT matrix $\boldsymbol{S}$ are generated by each channel as discussed in Section 2.2. By applying (9) to each $\boldsymbol{x}_j$, a coloured-MT version of the corresponding DFT is then derived as

$$f_{\mathrm{CMT}_j} = \boldsymbol{F} x_{\mathrm{CMT}_j} = \boldsymbol{F}\boldsymbol{C} x_{\mathrm{MT}_j} = \boldsymbol{F}\boldsymbol{C}_j\boldsymbol{S}\boldsymbol{x}_j, \tag{15}$$

As both $\boldsymbol{x}_j$ and $\boldsymbol{y}$ are $N \times 1$ vectors, $\boldsymbol{y}$ in (14) can be expressed in vector form by using (15)

$$\begin{aligned}
\boldsymbol{y} = \sum_{j=1}^{J} \boldsymbol{\Phi}_J \boldsymbol{x}_j &= [\Phi_1 \quad \Phi_2 \quad . \quad . \quad \Phi_J] \begin{bmatrix} x_1 \\ x_2 \\ . \\ . \\ x_J \end{bmatrix} \\
&= [\Phi_1 \quad \Phi_2 \quad . \quad . \quad \Phi_J] \begin{bmatrix} \boldsymbol{S}^{-1}\boldsymbol{C}_1^{-1}\boldsymbol{F}^{-1} f_{\mathrm{CMT}_1} \\ \boldsymbol{S}^{-1}\boldsymbol{C}_2^{-1}\boldsymbol{F}^{-1} f_{\mathrm{CMT}_2} \\ . \\ . \\ \boldsymbol{S}^{-1}\boldsymbol{C}_J^{-1}\boldsymbol{F}^{-1} f_{\mathrm{CMT}_J} \end{bmatrix} \\
&= [\Phi_1 S^{-1} C_1^{-1} F^{-1} \quad . \quad . \quad \Phi_J S^{-1} C_J^{-1} F^{-1}] \begin{bmatrix} f_{\mathrm{CMT}_1} \\ f_{\mathrm{CMT}_2} \\ . \\ . \\ f_{\mathrm{CMT}_J} \end{bmatrix} \\
&= [G_{\mathrm{CMT}_1} \quad . \quad . \quad G_{\mathrm{CMT}_J}]\, \boldsymbol{q} = \boldsymbol{G}_{\mathrm{CMT}}^{\mathrm{CM}}\, \boldsymbol{q},
\end{aligned} \tag{16}$$

where $\boldsymbol{G}_{\mathrm{CMT}}^{\mathrm{CM}}$ is the concatenation of matrices $\boldsymbol{\Phi}\boldsymbol{S}^{-1}\boldsymbol{C}_j^{-1}\boldsymbol{F}^{-1}$ and vector $\boldsymbol{q}$ is the combined PM-MT representation of signals $x_1, x_2, \ldots, x_J$ in the Fourier domain. The complete block diagram for the UNI-CM architecture is shown in Fig. 3.

The sparsity basis for the CM model in (16) is a $JN \times JN$ block diagonal matrix with $N \times N$ bases $\boldsymbol{F}$ along the diagonal [22], with the sparsity basis for each individual $\boldsymbol{x}_j$ being $\boldsymbol{F}$. Thus, the CS solution requires determining $\boldsymbol{q}$ using (16).

As with the RD, integrating precolouring and MT estimation leads to a unified UNI-CM architecture that combines the advantages of both sparsity enhancement algorithms, so it is similarly effective for digital modulation schemes and narrowband signals.

Interestingly, (16) reveals that the computational complexity of the UNI-CM architecture is again dependent upon the number of Slepian sequences N and precolouring filter order p employed. The key difference, however, between the two unified architectures lies in their processing structure. In UNI-RD, there are multiple concurrent processing branches and subsequent PSD recovery before a final summation. In UNI-CM, the summation is performed prior to the recovery process, which involves solving multiple equations similar in nature to (11).

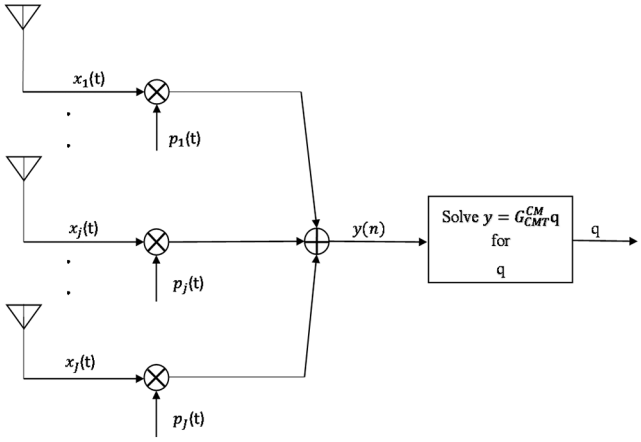

Fig. 3 *Block diagram of the J-channel UNI-CM architecture*

In terms of hardware complexity, because the UNI-CM is parallel architecture, its ability to sense a wider frequency spectrum is correspondingly enhanced compared with UNI-RD.

The respective spectral classification performance of both the UNI-RD and UNI-CM architectures will now be evaluated, with a novel tristate classifier being introduced.

4 Tristate spectral classifier

CR spectrum sensing extends beyond deriving a signal PSD, since the key objective is to assign an occupancy state to every band. Traditional spectral classification involves a binary hypothesis test [41] and a detection metric [3, 41], so if the signal energy in a band exceeds a predefined threshold, then it is occupied and assigned a black status, otherwise, it is classified as vacant (white). This implicitly assumes only two possible states exist for a band, while in [3, 8] a third state, the so-called *grey state* is proposed. One scenario that illustrates grey-band occupancy [8] is the presence of multiple *Code Division Multiple Access* (CDMA) signals, where either one or more CDMA signals is underutilised, so the CR can opportunistically exploit these for SU access without introducing harmful interference [43, 44]. Another example is digital TV, where interfering signals with widely varying power levels are present despite the PU, the broadcaster, being switched off [8]. Grey bands also exist in mobile networks, where interference is produced from the base station transmissions of different providers in the same service area [8]. All these examples involve a weak PU signal that can render the relevant channel potentially available for SU access under stringent interference constraints. In the two-band occupancy solution, grey bands are always classified as occupied so no SU access is feasible with a causal impact on the overall spectral efficiency.

In the tristate spectral classification, two energy thresholds T_1 and T_2 are defined, which, respectively, determine the existence of either a vacant band or occupied frequency. Intermediate values characterise the grey bands. In general, the spacing between T_1 and T_2 is location-specific, so it will be notably narrower in a building environment than in an outdoor line-of-sight situation [3], which is the scenario considered in this discussion. T_1 is set to the average input noise level, so if the average energy within a spectral band is less than T_1, then only noise is present, and it is deemed vacant for SU access. T_1 is defined as

$$T_1 = \frac{P}{1 + 10^{\mathrm{SNR}/10}}, \tag{17}$$

where SNR is the measured input to signal-to-noise ratio and P is the signal plus noise power over the signal duration t.

Table 1 OFDM test signal parameters

Parameter	LTE	IEEE 802.11.af	IEEE 802.116	IEEE 802.22
no of sub-carriers	181	144	256	2120
sub-carrier spacing, Hz	16,575	41,667	13,672	3300
OFDM symbol duration	1/16575	1/41667	1/13672	1/3300
OFDM channel bandwidth	3	6	3.5	7

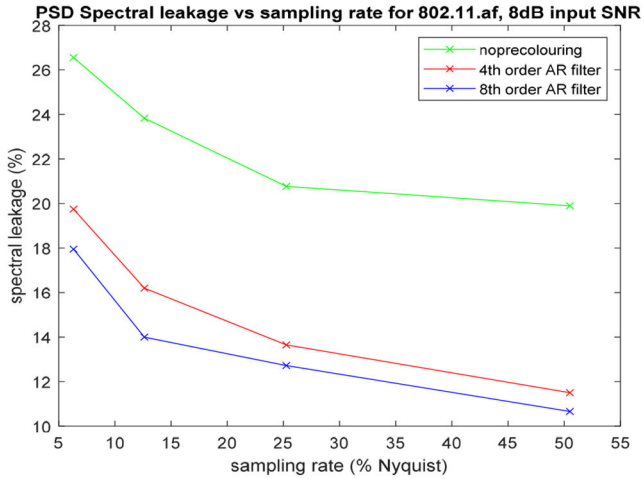

Fig. 4 *PSD spectral leakage versus sampling rate for IEEE 802.11.af*

To set T_2, because the signals of interest are generally frequency sparse, the average signal power is an inappropriate metric because it can be lower than the average power in occupied bands. Instead, the *root mean square* (RMS) value of the signal PSD is used because it provides a higher value than the average power and is closer to that of the occupied bands. Indeed, the greater the sparsity, the lower the RMS so if the average energy in a band is more than T_2, then the band is occupied. The signal power P, SNR and RMS parameter values are all measured and monitored using conventional spectrum analysis, which means both T_1 and T_2 can be adaptively determined according to the desired classification performance.

To determine the power in each band, it is assumed all bands have the same bandwidth b with the input signal having a baseband width of B and known PSD produced by either the UNI-RD or UNI-CM architectures. If the frequency resolution is Δf, then $B = N\Delta f$ and $b = K\Delta f$, where N is the number of signal samples at the Nyquist rate and K the number of frequencies resolved within a band. It is also assumed the occupancy status assigned to a specific band applies to all frequencies, so for an occupied band, all frequencies within b are occupied and none available to be used as a SU carrier frequency. The total power within a band having a centre frequency f_j is then

$$E(f_j) = \sum_{j-(K/2)+1}^{j+(K/2)} P(f_j)\Delta f, \tag{18}$$

where $= K/2, \ldots, N - K/2$, and $P(f_j)$ is the PSD value at a frequency f_j, which is constant for a given resolution Δf.

A *frequency classification vector* $\boldsymbol{v}_{\mathrm{CS}}$ comprising entries corresponding to the centre frequencies f_j is formed, which assigns values 1, 0 and ½, respectively, to an occupied, vacant and grey frequency. A *reference vector* $\boldsymbol{v}_{\mathrm{ref}}$ represents the actual occupancy state of B, where all active carrier frequencies are a 1 with all the other frequencies a 0. In the ideal scenario, band occupancy will be known so there are no grey frequencies. The spectral classification accuracy is then the Euclidean distance (l_2 norm) between $\boldsymbol{v}_{\mathrm{CS}}$ and $\boldsymbol{v}_{\mathrm{ref}}$ and a similarity metric $s(\boldsymbol{v}_{\mathrm{CS}}, \boldsymbol{v}_{\mathrm{ref}})$ formulated as

$$s(\boldsymbol{v}_{\mathrm{CS}}, \boldsymbol{v}_{\mathrm{ref}}) = \frac{1}{||\boldsymbol{v}_{\mathrm{CS}} - \boldsymbol{v}_{\mathrm{ref}}||_2}, \tag{19}$$

The rationale behind $s(\boldsymbol{v}_{\mathrm{CS}}, \boldsymbol{v}_{\mathrm{ref}})$ is that signal bandwidth, frequency and occupancy state are analogous to images, pixels and brightness levels in an image processing context. So signal bandwidth is a vector whose individual entries represent the occupancy state of each corresponding frequency. The higher the value of $s(\boldsymbol{v}_{\mathrm{CS}}, \boldsymbol{v}_{\mathrm{ref}})$ in (19), the better the classification accuracy and thereby the CS performance of each respective unified architecture.

There are signalling overheads incurred as a result of feedback mechanism to inform the SU about the opportunist availability of spectral bands, though this will be negligibly small in both architectures. This task can be undertaken by the tristate spectral classifier, which assigns occupancy status for each of the bands and transmits this information to the SU. The cost is dependent on the number of bits used to represent the occupancy status, which in this scenario is 2 bits, the number of the bands and the SU information update rate. Thus, the indicative signalling overheads will be $\simeq (2B/b) \times$ update rate, which pragmatically, is negligibly small.

5 Experimental setup

A critical performance evaluation of the UNI-RD and UN-CM architectures is now presented for OFDM signals. The OFDM test signal parameter settings are given in Table 1, with all values being fully compliant with four wireless standards LTE, IEEE 802.11af, IEEE 802.16 and IEEE 802.22 so ensuring all test signals used are as near as possible to real-world scenarios. Additive white Gaussian noise is added to all test signals. It is assumed the CR receiver sparse bandwidths of ≃34 MHz for LTE and IEEE 802.16 and ≃43 MHz for IEEE 802.11af and IEEE 802.22. In all scenarios, the locations of the channel and carrier frequencies are unknown, and each channel or carrier corresponds to a different PU. The relevant AR precolouring coefficients are assumed available to the CR receiver, with experiments performed using both 4th and 8th filter orders as in [36]. All experiments were performed on a MATLAB-based computing platform, using an HP Pavilion G6 Notebook, Intel Core-i5 AT 2.4 GHz, 4 GB RAM.

Two metrics are used to comparatively evaluate the CS performance of the UNI-RD and UNI-CM architectures. PSD spectral leakage measurements over a range of sub-Nyquist sampling rates and input signal noise robustness [35, 36]. The rationale for the former is that low spectral leakage reflects enhanced signal sparsity as fewer active components are present. It also means a favourable bias-variance and superior spectral estimate [30].

6 Results discussion

The respective PSD spectral leakage performances of both the UNI-RD and original RD architectures for the wireless standards mentioned above are shown in Figs. 4–7 for an input SNR of 8 dB [38]. It is evident for all four test signals that the PSD spectral leakage using precolouring is consistently lower across the range of sampling rates, providing an overall spectral leakage improvement of ≃33%. For UNI-RD, the average spectral leakage is consistently <20% compared to being always >15% for the original RD model. Furthermore, eighth-order precolouring gives an additional 10% leakage improvement for UNI-RD over the fourth-order AR filter.

To critically assess the robustness of the UNI-RD architecture, comparative results with the original RD model are displayed in Figs. 8–11 for a range of input SNR values at a sampling rate of 25.25% of the Nyquist frequency. As shown in Fig. 4, spectral leakage is consistently lower for the eighth-order UNI-RD, with an average improvement of ≃50%, with UNI-RD providing a further ≃ 13% enhancement compared to its fourth-order counterpart. Enhanced CS robustness of UNI-RD is readily apparent as the SNR degrades, while at higher input SNR, the respective CS performances are similar.

Similar spectral leakage trends are evident in Figs. 12–15 for the UNI-CM architecture. Comparing the fourth-order UNI-CM with the original CM model, the PSD spectral leakage is nearly

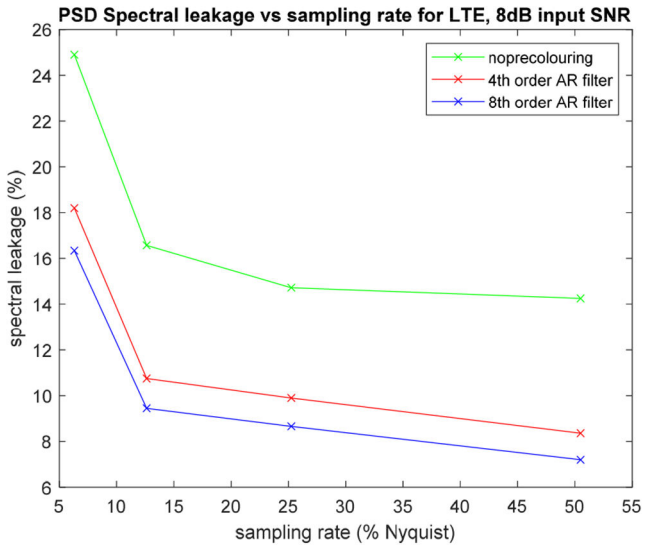

Fig. 5 *PSD spectral leakage versus sampling rate for LTE*

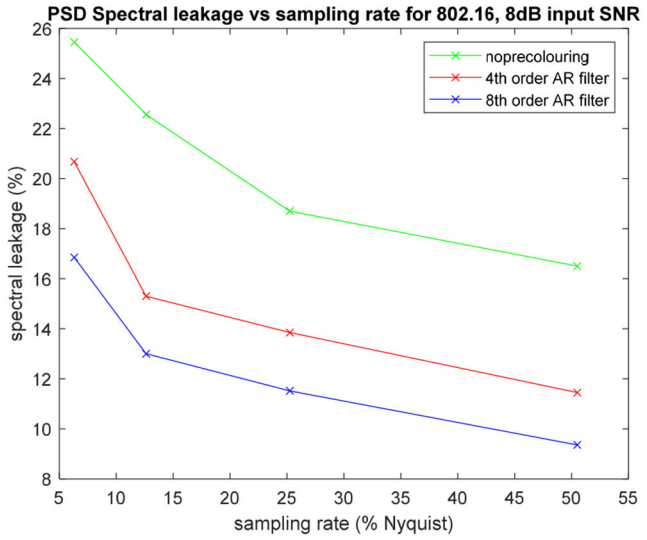

Fig. 6 *PSD spectral leakage versus sampling rate for IEEE 802.16*

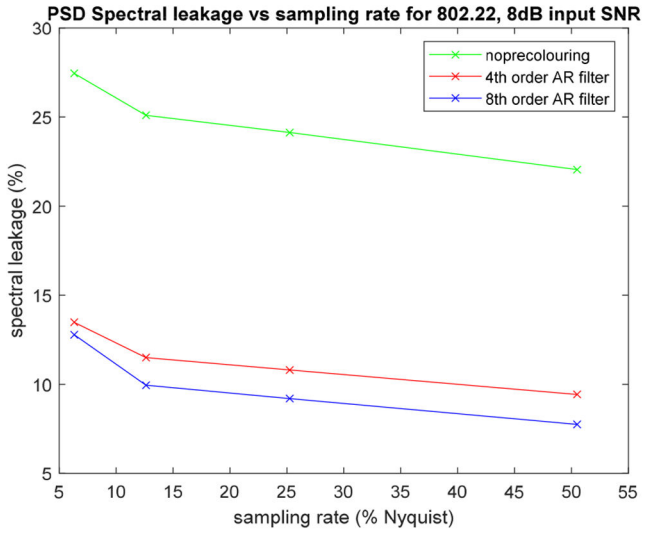

Fig. 7 *PSD spectral leakage versus sampling rate for IEEE 802.22*

50% better across the input SNR range, while using an eighth-order UNI-CM model gives a further ≃15% improvement. Note, the CS performance of both the unified architectures is superior when an eighth-order AR precolouring filter is used, though conversely, the

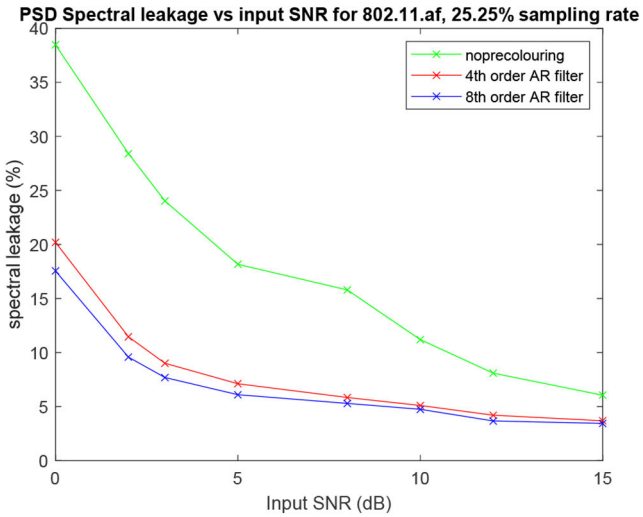

Fig. 8 *PSD spectral leakage versus input SNR for IEEE 802.11.af*

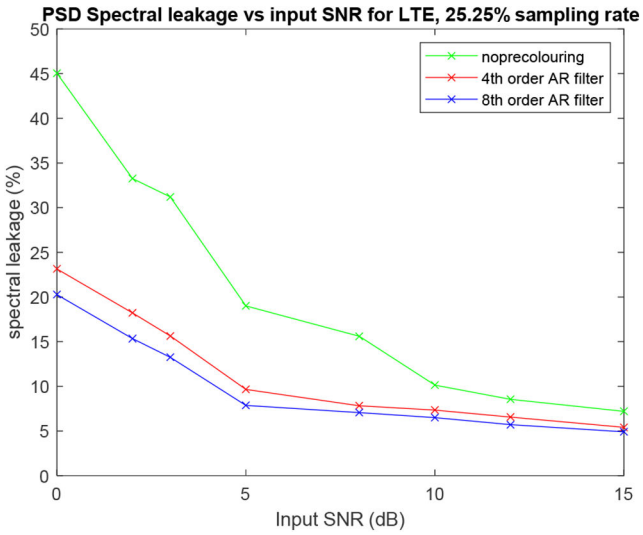

Fig. 9 *PSD spectral leakage versus input SNR for LTE*

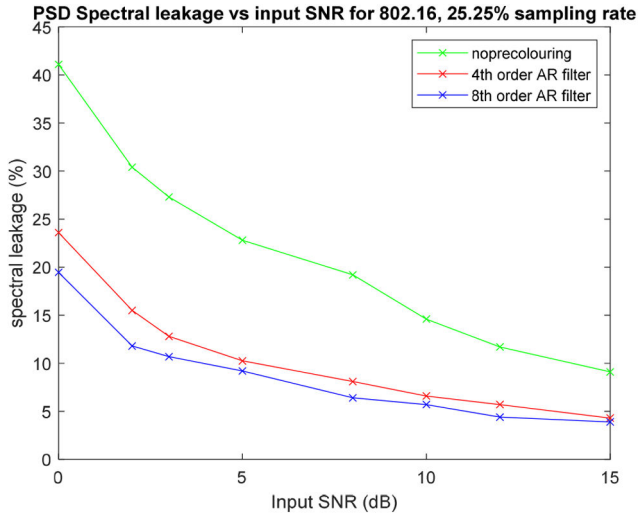

Fig. 10 *PSD spectral leakage versus input SNR for IEEE 802.16*

fourth-order solution provides a pragmatic design trade-off between CS complexity and latency.

The consistently superior CS results for both UNI-RD and UNI-CM are firmly predicated upon the inherent sparsity enhancement capability derived by precolouring the input signal. Similarly, these architectures increase sparsity and, thus, CS performance, for narrowband signals, where the AR coefficients are unavailable.

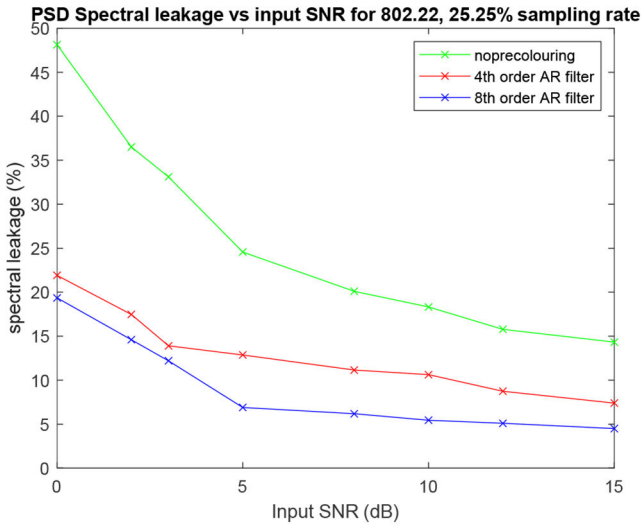

Fig. 11 *PSD spectral leakage versus input SNR for IEEE 802.22*

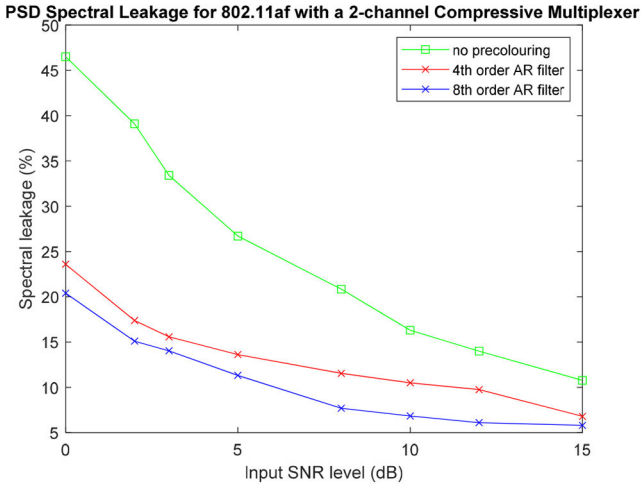

Fig. 12 *PSD spectral leakage versus input SNR for IEEE 802.11.af, UNI-CM architecture*

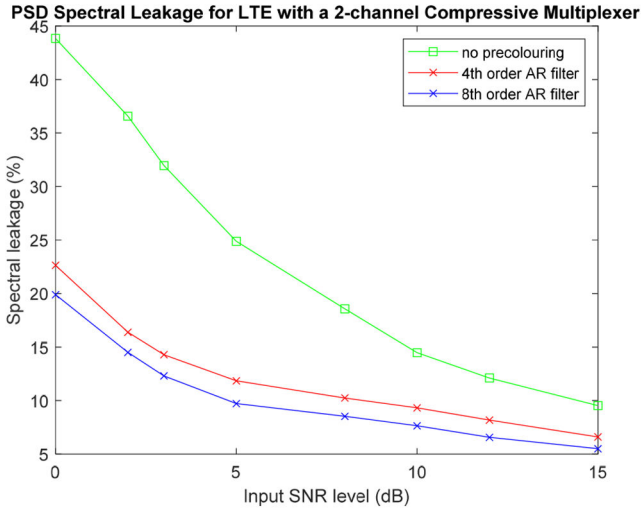

Fig. 13 *PSD spectral leakage versus input SNR for LTE, UNI-CM architecture*

To illustrate the key role the MT estimator has in both UNI-RD and UNI-CM architectures for CS of narrowband type signals like AM, Figs. 16 and 17 present the corresponding spectral leakage results at various sampling rates and input SNR values. Again, the spectral leakage performance is consistently better for both unified models, to corroborate the fact that by using the MT estimator

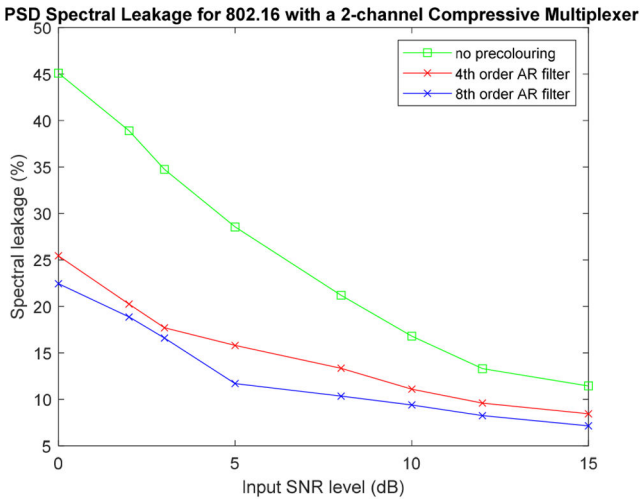

Fig. 14 *PSD spectral leakage versus input SNR for IEEE 802.16, UNI-CM architecture*

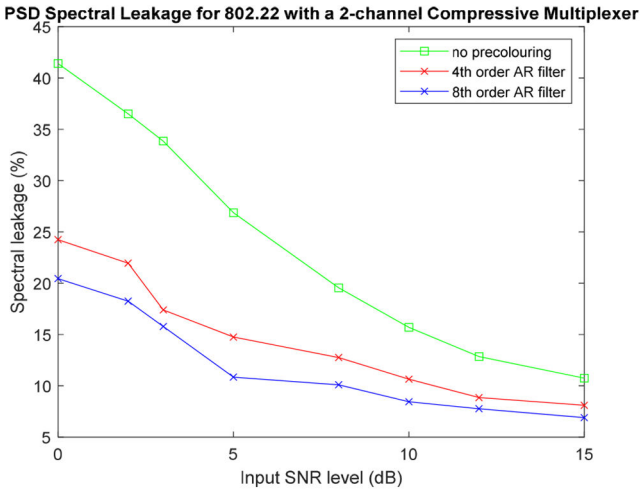

Fig. 15 *PSD spectral leakage versus input SNR for IEEE 802.22, UNI-CM architecture*

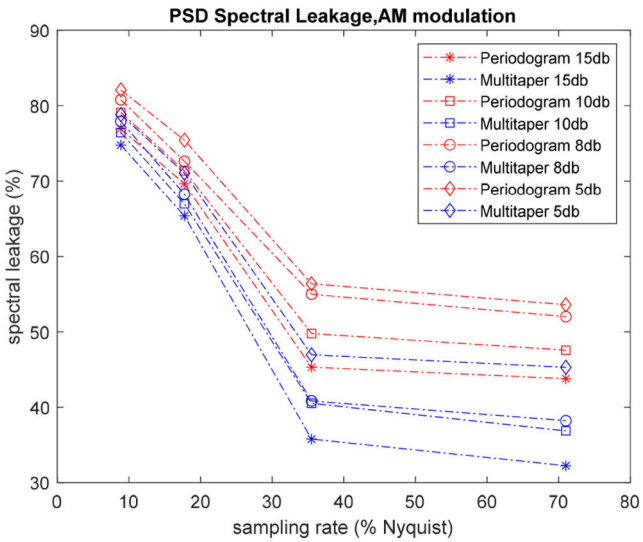

Fig. 16 *Comparative impact of the MT method on PSD spectral leakage for the UNI-RD*

instead of the periodogram achieves both enhanced signal sparsity and improves CS.

To critically evaluate the role of the tristate spectral classifier in the new unified architectures, the respective classification performances for UNI-RD and UNI-CM are shown in Figs. 18–21,

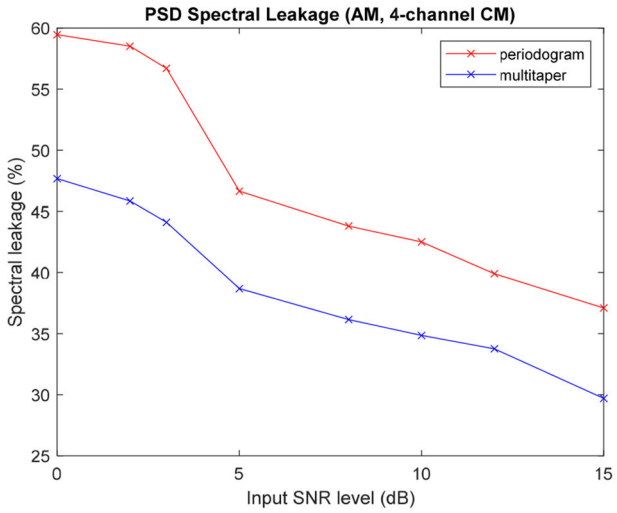

Fig. 17 *Comparative impact of the MT method on PSD spectral leakage for the UNI-CM*

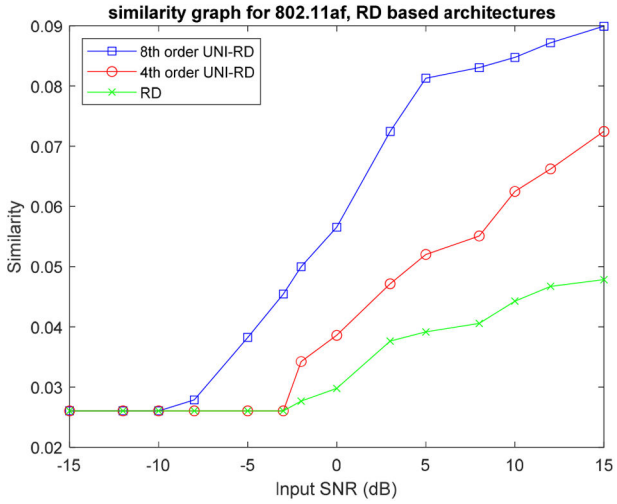

Fig. 18 *Spectral classification performance comparison for UNI-RD and RD architectures for IEEE 802.11af*

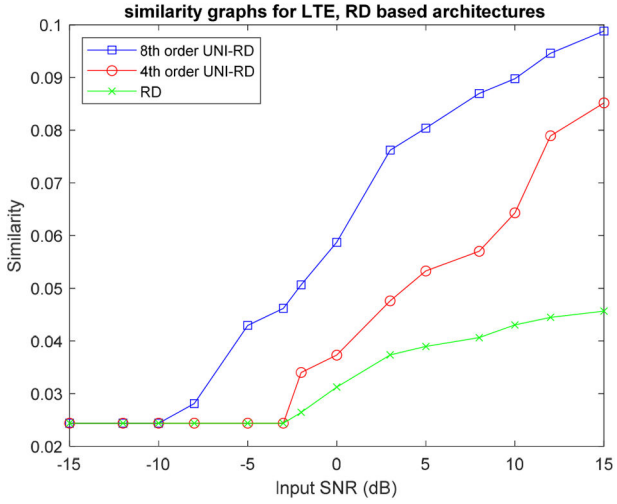

Fig. 19 *Spectral classification performance comparison for UNI-RD and RD architectures for LTE*

respectively. In both cases, the *similarity metric* ($\boldsymbol{\nu}_{\mathrm{CS}}$ $\boldsymbol{\nu}_{\mathrm{ref}}$) in (19) is plotted for IEEE 802.11.af, LTE and IEEE 802.16, IEEE 802.22, respectively, as a function of input SNR and at a sub-sampling rate of 25.5% of Nyquist.

The results validate that introducing a third grey-state significantly enhances the classification performance of both UNI-RD and UNI-CM architectures, so affording superior channel sensing and decision-making capability. This is attributable to the fact that in cases where the classification vector is assigned a grey state value of 1/2, it is significantly closer to the vacant state, so the CR is better able to identify and exploit SU access opportunities.

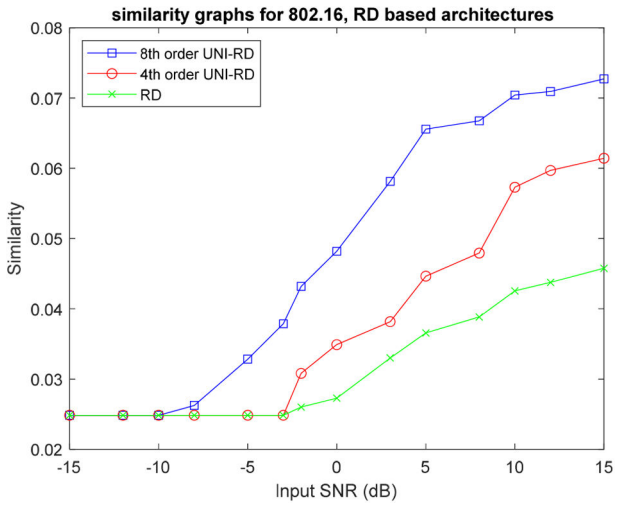

Fig. 20 *Spectral classification performance comparison for UNI-CM and CM architectures for IEEE 802.16*

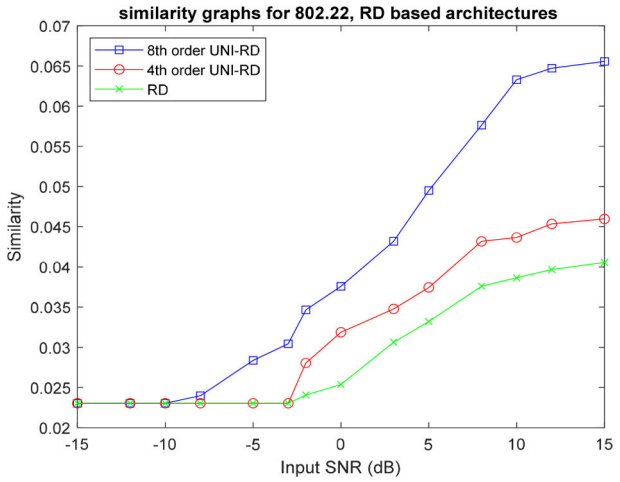

Fig. 21 *Spectral classification performance comparison for UNI-CM and CM architectures for IEEE 802.22*

Recalling a high $s(\boldsymbol{\nu}_{\mathrm{CS}}, \boldsymbol{\nu}_{\mathrm{ref}})$ in (19) implies superior spectrum classification accuracy, it can be observed that all the various plots in Figs. 18 and 19 converge to a minimum similarity distance with, for example the UNI-RD (fourth-order) having a minimum $s(\boldsymbol{\nu}_{\mathrm{CS}}, \boldsymbol{\nu}_{\mathrm{ref}}) \simeq 0.025$ at an SNR threshold of -3 dB. The results interestingly reveal that while the fourth-order UNI-RD performs better at higher SNR values, eighth-order UNI-RD is more robust, converging to the same minimum $s(\boldsymbol{\nu}_{\mathrm{CS}}, \boldsymbol{\nu}_{\mathrm{ref}})$ value, but at a lower SNR threshold of -10 dB. Similar observed performance trends are evident for the corresponding UNI-CM architectures in Figs. 20 and 21.

7 Conclusion

Existing *CS* architectures are generally constrained in their spectrum sensing ability for *CR* applications by the wide range of available wireless signal types and access schemes that are used. To address these limitations, this paper has presented two novel unified CS architectures, namely UNI-RD and UNI-CM, which seamlessly integrate precolouring and the *multitaper* spectral estimator into their designs to enhance signal sparsity and extend their CS capability for both narrowband and digitally modulated schemes including complex CR-related access technologies like *OFDM*. The extensive critical evaluation has validated the

improved CS performance achieved by both architectures into which a tristate spectral classification regime has been integrated, which demonstrably offers significant new spectral access opportunities for CR *SUs*.

Future work will focus upon extending these unified architectures to other CS models and framing a strategy for automatically determining the thresholds for the new tristate spectral classifier.

8 References

[1] 'Cisco virtual networking index: global mobile data traffic forecast update', CISCO White Paper, 2016

[2] 'Cisco virtual networking index: forecast and methodology 2016–2021', CISCO White Paper, 2016

[3] Ekram, H., Vijay, B.: 'Cognitive wireless communications', 2007

[4] F. C. Commission: 'Spectrum policy task force', ET Docket 02-135, 2002

[5] Broderson, R., Wolisz, A., Cabric, D., *et al.*: 'CORVUS: A cognitive radio approach for usage of virtual unlicensed spectrum'. University of Berkeley, 2004

[6] Lunden, J., Koivunen, V., Poor, V.: 'Spectrum exploration and exploitation for cognitive radio', *IEEE Signal Process. Mag.*, 2015, **32**, pp. 123–140

[7] Sun, H., Nallanathan, A., Wang, C.: 'Wideband spectrum sensing for cognitive radio networks', *IEEE Wirel. Commun.*, 2013, **20**, pp. 74–81

[8] Haykin, S., Reed, D.: 'Spectrum sensing for cognitive radio', *IEEE Proc.*, 2009, **97**, (5), pp. 849–877

[9] Arjoune, Y., Kaabouche, N.: 'A comprehensive survey on spectrum sensing in cognitive radio networks: recent advances, new challenges, and future research directions', *Sensors*, 2019, **19**, (126), pp. 1–32

[10] Abedi, M.R., Mokari, N., Javan, M.R., *et al.*: 'Secure communication in OFDMA-based cognitive radio networks: an incentivized secondary network coexistence approach', *IEEE Trans. Veh. Technol.*, 2017, **66**, (2), pp. 1171–1185

[11] Zhang, W., Wang, C.X., Chen, Y.: 'Enhanced 5G cognitive radio networks based on spectrum sharing and spectrum aggregation', *IEEE Trans. Commun.*, 2018, **66**, pp. 6304–6316

[12] Ghasemi, A., Sousa, E.: 'Spectrum sensing in cognitive radio networks: requirements, challenges and design trade-offs', *IEEE Commun. Mag.*, 2008, **46**, (4), pp. 32–39

[13] Tian, Z., Giannakis, G.: 'Compressed sensing for wideband cognitive radios'. IEEE Int. Conf. on Acoustics, Speech, and Signal Processing (ICASSP), Honolulu, HI, USA, 2007, pp. V1357–IV1360

[14] Candès, E., Romberg, J., Tao, T.: 'Robust uncertainty principles: exact signal recovery from highly incomplete frequency information', *IEEE Trans. Inf. Theory*, 2006, **52**, (2), pp. 489–509

[15] Donoho, D.: 'Compressed sensing', *IEEE Trans. Inf. Theory*, 2006, **52**, (4), pp. 1209–1308

[16] 'An introduction to compressive sensing', 2020. Available at http://cnx.org/content

[17] Candès, E., Walkin, M.: 'An introduction to compressive sampling', *IEEE Signal Process. Mag.*, 2008, **52**, (4), pp. 21–30

[18] Sharma, S.K., Lagunas, E., Chatzinotas, S., *et al.*: 'Application of compressive sensing in cognitive radio communications: a survey', *IEEE Commun. Surv. Tutor.*, 2016, **18**, pp. 1838–1860

[19] Salahdine, E., Kaabouch, N., El Ghazi, E., *et al.*: 'A survey on compressive sensing techniques for cognitive radio networks', *J. Phys. Commun.*, 2016, **20**, pp. 61–73

[20] Tropp, J., Laska, J., Duarte, M., *et al.*: 'Beyond Nyquist: efficient sampling of sparse bandlimited signals', *IEEE Trans. Inf. Theory*, 2010, **56**, (1), pp. 520–544

[21] Eldar, Y., Kutyniok, G.: '*Compressed sensing: theory and applications*' (Cambridge University Press, USA, 2015)

[22] Slavinsky, J., Laska, J., Davenport, M., *et al.*: 'The compressive multiplexer for multi-channel compressive sensing'. IEEE Int. Conf. on Acoustics, Speech, and Signal Processing, Prague, Czech Republic, 2011, pp. 3980–3983

[23] Romberg, J.: 'Sensing by random convolution'. IEEE Workshop in Computational Advances in Multi-sensor Adaptive Processing, St. Thomas, VI, USA, 2007, pp. 137–140

[24] Tropp, J., Wakin, M., Duarte, M., *et al.*: 'Random filters for compressive sampling and reconstruction'. IEEE Int. Conf. on Acoustics, Speech, and Signal Processing, Toulouse, France, 2006, pp. 872–875

[25] Ragheb, T., Laska, J., Najati, H., *et al.*: 'A prototype prototype analog-to-digital conversion'. 51st Midwest Symp. on Circuits and Systems, Knoxville, TN, USA, 2008, pp. 37–40

[26] Mishali, M., Eldar, Y., Dounaevsky, O., *et al.*: 'Xampling: analog to digital at sub-Nyquist rates', *IET Circuits Devices Syst.*, 2011, **5**, (1), pp. 8–20

[27] Yu, Z., Hoyos, S.: 'Compressive spectrum sensing front-ends for cognitive radios'. IEEE Int. Conf. on Systems, Man and Cybernetics, San Antonio, TX, USA, 2009, pp. 1899–1904

[28] Taheri, O., Vorobyov, A.: 'Segmented compressed sampling for anaolg-to-information conversion: method and performance analysis', *IEEE Trans. Signal Process.*, 2011, **59**, (2), pp. 554–572

[29] Lu, Y., Guo, W., Wing, X., *et al.*: 'Distributed streaming compressive spectrum sensing for wideband cognitive radio networks'. 73rd Vehicular Technology Conf., Budapest, Hungary, 2011, pp. 1–5

[30] Manolakis, D., Ingle, V., Kogon, S.: '*Statistical and adaptive signal processing: spectrum estimation signal modeling*' (Artech House, USA, 2005)

[31] Madisetti, V: '*The digital signal processing handbook*' (CRC Press, 2010, USA, 2nd edn.)

[32] Zhao, L., Chen, X., Zhang, G.: 'A novel spectrum sensing algorithm based on compressive sensing for cognitive radio'. IEEE Workshops of Int. Conf. on Advanced Information Networking and Applications, Biopolis, Singapore, 2011, pp. 243–246

[33] Harms, A., Bajwa, R., Calderbank, R.: 'A constrained random demodulator for sub-Nyquist sampling', *IEEE Trans. Signal Process.*, 2013, **61**, (3), pp. 707–723

[34] Mangia, M., Rovatti, R., Setti, G.: 'Analog-to-information'. IEEE Int. Symp. of Circuits and Systems Conversion of Sparse and Non-White Signals: Statistical Design of Sensing Waveforms, Rio de Janeiro, Brazil, 2011, pp. 2129–2132

[35] Karampoulas, D., Dooley, L., Kouadri, S.: 'A multitaper random demodulator model for narrowband compressive spectral estimation'. IEEE GlobalSIP, Orlando, FL, USA, 2015, pp. 1362–1366

[36] Karampoulas, D., Dooley, L., Kouadri, S.: 'Integration of a precolouring matrix in the random demodulator model for improved compressive spectrum estimation'. IEEE GlobalSIP, Atlanta, GA, USA, 2014, pp. 1209–1213

[37] 3GPP: 'The mobile broadband standard'. Available at http://www.3gpp.org

[38] Flores, A., Guerra, R., Knightly, E.: 'IEEE 802.11af: a standard for TV white space spectrum sharing', *IEEE Commun. Mag.*, 2013, **51**, (10), pp. 92–100

[39] 'IEEE 802.16-2017-IEEE standards for air interface for', IEEE 802.16 Working Group. Available at https://standard.ieee.org.standard/802_16-2017. Accessed 04 March 2019

[40] 'IEEE 802.22 Working Group on wireless regional area'. Available at http://www.ieee802.org/22. Accessed 05 March 2019

[41] Akyildiz, I., Lo, B., Balakrishnan, R.: 'Cooperative spectrum sensing for cognitive radio networks', *J. Phys. Commun.*, 2011, **4**, pp. 40–62

[42] Marple, S.: '*Digital spectral analysis with applications*' (Prentice-Hall, USA, 1987)

[43] Fette, B.: '*Cognitive radio technology*' (Elsevier, USA, 2009)

[44] Mody, A., Blatt, S.R., Mills, D.G., *et al.*: 'Recent advances in communications', *IEEE Commun. Mag.*, 2007, **45**, (10), pp. 54–61